3D printed stretchable triboelectric nanogenerator fibers and devices

Yuxin Tong, Ziang Feng, Jongwoon Kim, John L. Robertson, Xiaoting Jia, Blake N. Johnson

PII: S2211-2855(20)30550-4

DOI: https://doi.org/10.1016/j.nanoen.2020.104973

Reference: NANOEN 104973

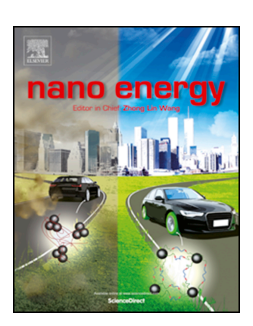
To appear in: Nano Energy

Received Date: 13 March 2020 Revised Date: 30 April 2020 Accepted Date: 17 May 2020

Please cite this article as: Y. Tong, Z. Feng, J. Kim, J.L. Robertson, X. Jia, B.N. Johnson, 3D printed stretchable triboelectric nanogenerator fibers and devices, *Nano Energy* (2020), doi: https://doi.org/10.1016/j.nanoen.2020.104973.

This is a PDF file of an article that has undergone enhancements after acceptance, such as the addition of a cover page and metadata, and formatting for readability, but it is not yet the definitive version of record. This version will undergo additional copyediting, typesetting and review before it is published in its final form, but we are providing this version to give early visibility of the article. Please note that, during the production process, errors may be discovered which could affect the content, and all legal disclaimers that apply to the journal pertain.

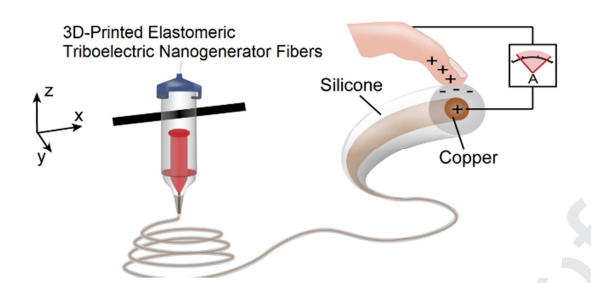
© 2020 Published by Elsevier Ltd.



## **Author Contributions**

YT, ZF, XJ, and BNJ conceived the concept of 3D printable elastomeric metal-core multifunctional fibers. YT and BNJ created the triboelectric fiber 3D printing process. YT and ZF designed and fabricated the fibers and devices. ZF, JK, and YT performed the characterization studies, data analysis, and supervised learning. JR, YT, and BNJ designed the organ monitoring studies and analyzed the organ edema data. YT, ZF, XJ, and BNJ conceived concepts of monitoring organ deformations and 'silent speech' via triboelectric sensing. YT, ZF, XJ, and BNJ organized, wrote, and edited the manuscript.

## **Graphical Abstract**



## 3D Printed Stretchable Triboelectric Nanogenerator Fibers and Devices

Yuxin Tong,<sup>‡1</sup> Ziang Feng,<sup>‡2</sup> Jongwoon Kim,<sup>2</sup> John L. Robertson,<sup>3</sup> Xiaoting Jia,<sup>2,5\*</sup> and Blake N. Johnson<sup>1,4-6\*</sup>

**Keywords:** 3D Printing; Conformal Printing; Bionics; Wearable Systems; Silent Speech; Organ Preservation

\*Co-Corresponding Authors:

Address: Department of Industrial and Systems Engineering, 250 Durham Hall, 1145 Perry Street, Blacksburg, VA 24061 USA. E-mails: xjia@vt.edu; bnj@vt.edu. Phones: 540-231-3065; 540-231-0755

<sup>&</sup>lt;sup>1</sup> Grado Department of Industrial and Systems Engineering, Virginia Tech, Blacksburg, VA 24061 USA

<sup>&</sup>lt;sup>2</sup> Bradley Department of Electrical and Computer Engineering, Virginia Tech, Blacksburg, VA 24060, USA

<sup>&</sup>lt;sup>3</sup> School of Biomedical Engineering and Sciences, Virginia Tech, Blacksburg, VA 24061 USA

<sup>&</sup>lt;sup>4</sup> Macromolecules Innovation Institute, Virginia Tech, Blacksburg, VA 24061 USA

<sup>&</sup>lt;sup>5</sup> Department of Materials Science and Engineering, Virginia Tech, Blacksburg, VA 24061 USA

<sup>&</sup>lt;sup>6</sup> Department of Chemical Engineering, Virginia Tech, Blacksburg, VA 24061 USA

<sup>&</sup>lt;sup>‡</sup> These authors contributed equally to this work.

### **Abstract**

Triboelectric generators and sensors have a great potential as self-powered wearable devices for energy harvesting, biomedical monitoring, and recording human activity. Here, we report a process for 3D printing stretchable membranes, meshes, and hollow 3D structures on planar, rotating, and non-planar anatomical substrates using elastomeric metal-core triboelectric nanogenerator (TENG) fibers. The triboelectric performance of single 3D-printed elastomeric metal-core silicone-copper (Cu) (cladding-core) fibers and 3D-printed membranes was quantified by cyclic loading tests, which showed maximum power densities of 31.39 and 23.94 mW m<sup>-2</sup>, respectively. The utility of the flexible silicone-Cu TENG fibers and 3D printing process was demonstrated through applications to wearable mechanosensors for organ and human activity monitoring, specifically, monitoring of perfused organs and speech recognition in the absence of sound production by the speaker (i.e., 'silent speech'), respectively. 3D-printed wearable triboelectric mechanosensors, in the form of stretchable form-fitting meshes and membranes, in combination with machine-learning signal processing algorithms, enabled realtime monitoring of perfusion-induced kidney edema and speech recognition in the absence of sound production by human subjects (99% word classification accuracy). Overall, this work expands the conductive and functional materials palette for 3D printing and encourages the use of 3D-printed triboelectric devices for self-powered sensing applications in biomanufacturing, medicine, and defense.

## **Highlights**

- Coaxial micro-extrusion process for production of flexible silicone-copper (cladding-core) triboelectric nanogenerator (TENG) fibers.
- 3D printing of stretchable triboelectric constructs and devices, including hollow 3D structures, membranes, and form-fitting wearable systems.
- Triboelectric-based real-time mechanosensing of organ edema and speech recognition in the absence of sound production by the speaker in combination with machine learning techniques.

### Introduction

The use of wearable electronics has grown substantially, owing to their promising applications, ranging from healthcare monitoring to communications[1-3]. However, conventional power sources, such as rechargeable electrochemical batteries, impose limitations on device weight, size, and usage time, which delay the development and deployment of practical and sustainable wearable electronics[1]. One promising path to overcome these limitations is self-powered electronic systems based on integrated energy-harvesting components. Triboelectric nanogenerators (TENGs) have gained considerable attention for their ability to convert mechanical to electrical energy, based on triboelectrification and electrostatic induction effects[1, 4-7]. Among the multiple forms of TENGs, fiber-based TENGs (FTENG) are attractive for various applications, given fibers are fundamental elements of complicated structures[8-17]. For example, fibers can be integrated and assembled into high-dimensional structures by processes such as weaving and knitting. However, existing FTENG fabrication approaches are often complex because of the involvement of multi-step coating and spinning processes[18-19]. Moreover, in many applications, form-fitting structures are desired for irregular shapes, which can be challenging to fabricate using traditional fiber assembly processes. For example, in organ monitoring applications, an anatomically-conforming mesh is preferable to planar textiles. However, it remains a challenge to fabricate stable high-dimensional devices with soft 1D fibers. Thus, new processes for the production and assembly of FTENG could create advanced triboelectric-based devices, such as by rapid prototyping of form-fitting wearable systems.

Multi-material 3D printing processes have been leveraged extensively for the fabrication of structural electronics[20-24], bionics[25-28], and wearable devices[29-32]. For example,

stereolithography processes have enabled the fabrication of gaming pieces composed of polymer-embedded electronics, including LEDs, microprocessors, accelerometers, and silver interconnects[21]. Micro-extrusion 3D printing processes have allowed the fabrication of bionic tissues and active 3D electronics, such as tissues that contain integrated stretchable antennas[25] and lenses containing integrated light-emitting diodes (LEDs)[33], respectively. However, the use of conductive and functional inks poses challenges to the design and fabrication of 3Dprinted TENG fibers and triboelectric devices because of high resistance, high cost, hightemperature post-processing steps (e.g., sintering), and poor mechanical properties, including limited flexibility and durability under cyclical loading[34]. Thus, it is desirable to expand the conductive and functional materials palette for 3D printing processes. To overcome the aforementioned limitations associated with the use of conductive and functional inks in electronics 3D printing, studies have been conducted to explore the feasibility of robotically interweaving high-quality drawn wires with 3D-printed constructs. For example, an integrated micro-extrusion 3D printing and pick-and-place process enabled the integration of platinum wires into silicone scaffolds, which was applied to the fabrication of custom-sized nerve cuffs[35-36]. A Fused Deposition Modeling process with active wire integration capabilities was developed for encapsulating conductive metal wires in an extrudable matrix of styrene block copolymers[34]. While important from the perspective of integrating high-quality wires (i.e., conducting materials) with 3D-printed constructs, the use of thermoplastics 12,17,18 makes the process relatively unattractive from the perspective of fabricating triboelectric devices (e.g., because of their poor performance as triboelectrically-negative materials and limited elasticity). In contrast, silicone rubber, a widely 3D-printed material in micro-extrusion processes [35-39], has been widely recognized as a promising candidate for use in triboelectric systems, due to its

high electronegativity, temperature-independent properties, resilience (i.e., long lifetime), and elasticity, which can generate a relatively large (and useful) charge upon contact with human skin through triboelectric effects[40-43]. However, it is currently difficult to achieve wire encapsulation within elastomeric materials, such as silicone.

Here, we present a fabrication process for the production and 3D printing of elastomeric metal-core silicone-copper (Cu) TENG fibers using a coaxial micro-extrusion process. Fabrication of 2D and 3D constructs - via 3D printing on stationary and moving substrates, including membranes, meshes, and hollow 3D structures - is demonstrated with capacitor charging and powering of LEDs. The utility of the flexible TENG fiber and 3D printing process is herein examined through applications to wearable mechanosensors to organ and human activity monitoring, specifically, monitoring of perfused organs and speech recognition in the absence of sound production by the speaker, which we refer to here as 'silent speech.' 3Dprinted mechanosensors, in the form of anatomical organ-conforming meshes, were leveraged for real-time monitoring of perfusion-induced kidney edema, a serious problem encountered in organ preservation and transplantation. We demonstrate that 3D-printed self-powered wearable mechanosensors in the form of stretchable membranes enable speech recognition in the absence of sound production and image-based facial expression monitoring by the speaker. These prototypic applications suggest that 3D-printed elastomeric metal-core silicone-Cu TENG fibers could provide the basis for development of high-performance triboelectric devices across a range of applications, including healthcare and human behavior monitoring, such as real-time monitoring of pain and 'silent speech'.

### **Materials and Methods**

Materials. Silicone (SI 595 CL) was from Loctite. Cu wire (bare uninsulated, 36 and 40 AWG) and Al wire (bare uninsulated, 28 AWG) was from WesBell Electronics, Inc. Glass pins (extra fine) were from Dritz. Polylactic acid 3D printing filament (PolyLite) was from Polymaker. Phosphate-buffered saline (PBS) was from Sigma Aldrich. Ultrapure deionized water (DIW) was from a commercially-available DIW system (Direct-Q 3UV; Millipore).

Customized manifolds design. Customized manifolds for 3D printing of elastomeric metal-core TENG fibers were designed with a computer-aided design (CAD) software (Onshape). Each manifold was designed as a hollow two-part structure. The top and bottom portions of the manifold served as a source of wire (core material) and die for passive wire feeding based on drag extruded silicone that surrounded the wire, respectively. The bottom portion of the manifold also served to provide structural integration with the surrounding dispensing barrel in which the elastomer was contained (see Supplementary Fig. S1a). The 3D design and engineering drawing of the customized manifold are shown in Supplementary Figs. S1b-c. The manifolds were fabricated using a commercially-available desktop 3D printer (LulzBot mini 2; LulzBot) using vendor-provided slicing software (Cura; LulzBot) and protocols (see Supplementary Fig. S1d-e).

Coaxial multi-material micro-extrusion 3D printing processes metal-core fibers. Elastomeric metal-core TENG fibers and devices were fabricated using a custom micro-extrusion 3D printing system, which consisted of a three-axis robot (MPS75SL; Aerotech), a digital pressure regulator (Ultimus V; Nordson), a motion controller (A3200; Aerotech), and coaxial extrusion nozzle (*i.e.*, dispensing barrel-manifold assembly). Cu wire (36 AWG), which served as the metallic core material, was first loaded on the top portion of the manifold. The preloaded manifold was then transferred into a dispensing barrel (10 cc; Nordson EFD), with a

18-gauge tapered tip. Silicone, which served as the elastomeric cladding material, was subsequently loaded in the coaxial extrusion barrel. Prior to printing, the metal core was anchored on the substrate by locally curing the cladding. TENG fibers were printed by continuous extrusion of silicone using a pressure of 15 psi at a constant vertical feed rate of 2 mm s<sup>-1</sup>. Following printing, the fibers were cured at room temperature. Fibers of varying composition are fabricated by changing the core material (28 AWG Al wire and 40 AWG Cu wire) and the printing nozzle diameter (16- and 20-gauge tapered tips) and appropriately modulating the extrusion pressure in the range of 10 - 20 psi.

Hollow 3D structures, specifically cylinders and cones, were fabricated by fiber 3D printing on continuously rotating glass mandrels (radius = 3 mm; frequency = 45 RPM) using a 16-gauge tapered tip and extrusion pressure of 20 psi. Following anchoring of the core material to the stationary mandrel, the structures were fabricated by fiber 3D printing with linear horizontal motion along the axial dimension of the mandrel in the presence of continuous mandrel rotation at 0.7 - 2 mm s<sup>-1</sup>. Wristbands were fabricated by fiber 3D printing on a rotating polylactic acid mandrel (radius = 70 mm; frequency = 45 RPM) using a 16-gauge tapered tip, extrusion pressure of 55 psi, and printing speed of 1.4 mm s<sup>-1</sup>. The printed structures were cured overnight prior to release from the mandrels.

Cuboid- and star-shaped 3D structures were fabricated on planar, stationary 3D-printed substrates that exhibited four and five anchoring pins, respectively (pin patterns are provided in Supplementary Fig. S1f and g, respectively). Substrates were designed using commercially-available CAD software and desktop 3D printer (Onshape and LulzBot mini 2, respectively) using vendor-provided slicing software (Cura; LulzBot) and protocols. The structures were 3D printed using an 18-gauge tapered tip, extrusion pressure of 15 psi, and printing speed of 2 mm s<sup>-1</sup>

<sup>1</sup> using a custom tool path. Changes in fiber trajectory during 3D printing were facilitated by fiber interweaving among the substrate anchoring pins by manual toolpath programming. The printed structures were cured overnight prior to release from the substrates.

TENG fiber-based membrane sensors for silent speech studies were printed on a planar substrate (see Supplementary Fig. S1h) that contained a  $50 \times 120 \times 3$  mm<sup>3</sup> cavity and 30 edge anchors using an 18-gauge tapered tip, extrusion pressure of 15 psi, and printing speed of 2 mm s<sup>-1</sup>. The toolpath consisted of a zig-zag pattern with a 45-degree inclination relative to the substrate edge. An additional layer of silicone was printed on top of the patch to smoothen the surface. The printed structures were cured overnight prior to release from the substrates.

TENG fiber-based mesh sensors for organ monitoring studies were conformally printed on 3D-printed models of porcine kidneys[39]. Conformal tool paths were manually programmed based on uniform mesh geometry that spanned the bottom half of the kidney. Glass pins were mounted to the kidney model to provide fiber anchor points within the non-planar tool path. Printing was performed using an 18-gauge tapered tip, extrusion pressure of 15 psi, and printing speed of 2 mm s<sup>-1</sup>. The printed structures were cured overnight prior to release from the substrates.

Characterization of 3D-printed TENG fibers and devices. The cross-section and the diameter of 3D-printed fibers were characterized using a microscope (Axio Zoom. V16; ZEISS). The active material was driven by a linear motor (LinMot E1200) in the cyclic loading tests, as shown in Supplementary Fig. S2. Fibers and wristbands were evaluated while clamped on a force plate (Vernier FP-BTA). The applied load was controlled using a sensor console (LabQuest 2) and the software (Logger Pro). Commercial acrylic plates (McMaster-Carr) were applied as moving materials. The moving frequency and contact force were maintained at 8 Hz and 50 N by

a linear motor. A programmable electrometer (Keithley 6514) was used to measure the short-circuit current, open-circuit voltage, transferred charge, and current in the quantitative electrical output and the self-powered sensors studies. The data were exported in real-time by a data acquisition card (National Instrument USB-6211), LabVIEW and Matlab.

A custom apparatus was used to investigate the effect of humidity on the TENG performance. A humidity sensor was placed adjacent to the fiber, which were both enclosed in an environment chamber that contained a humidifier. The sensor and the humidifier were connected to the humidity controller to achieve varying setpoints in the chamber humidity.

Characterization of perfusion-induced organ edema via real-time monitoring of 3D-printed TENG fiber-based devices. Adult porcine kidneys were obtained from a local abattoir in strict accordance with good animal practice as defined by the relevant national and local animal welfare bodies, and approved by Virginia Tech as previously reported[39]. Briefly, kidneys were dissected from the detached viscera and stored in an insulated container during transportation to the experiment site. The transportation time was 2 hours. Prior to machine perfusion, residual fat tissue around the organ was removed. The renal artery of the kidney was subsequently anastomosed to plastic tubing (7 mm diameter). The system tubing was then connected in series with a variable-speed peristaltic pump (Cole-Parmer) and feed reservoir that contained a PBS solution. Organ mechanosensing was done using 3D-printed TENG fiber-based mesh placed under the kidney, separated by a thin layer of insulating material (Parafilm). Data acquisition began five minutes prior to activating the perfusion process (*i.e.*, initiating the flow of PBS solution) to establish an initial baseline in the sensor response. Subsequently, the kidneys (n = 3) underwent normothermic perfusion for 1 hour in a single-pass flow mode using room temperature PBS solution as the perfusate at a flow rate of 7.8 mL min<sup>-1</sup>. Following the 1-hour

perfusion interval, the perfusate flow was stopped and the sensor response was continuously monitored for the next hour. Raw sensor data has been corrected by subtracting the baseline variation, in which the baseline was determined by the curve fitting of data acquired during the first five minutes (see Supplementary Fig. S3).

Characterization of perfusion-induced organ edema via real-time monitoring of 3D organ surface displacement. Perfused kidneys were continuously imaged from a top-down perspective over the course of the perfusion process using a single camera-projector structuredlight scanning system (HP 3D Structured Light Scanner Pro S3; HP). The system was calibrated in advance following vendor-provided protocols using a 60 mm calibration grid. collected every two minutes throughout the perfusion process, which resulted in a set of point clouds that quantify the out-of-plane displacement of the kidney during perfusion. The transient displacement was calculated as the distance between the first scan and subsequent scans. Quantification of the separation distance between two point clouds was performed using a commercially-available 3D CAD modeling software (Rhino 6; Rhinoceros). Specifically, a point object (P) was manually created above the point clouds  $(S_i)$ , which marked the location of the midpoint of the organ in the x- and y-axes based on top-down projection. Following projection of the same point on each scan using the Project command (i.e., the projection of point P on scan  $S_i$ resulted in the point  $P_i$ ), the absolute organ surface displacement (d) of scan  $S_i$  was then defined as the distance between the projected point  $P_i$  and  $P_{\theta}$ , where  $P_{\theta}$  is the projection of point P on the initial scan  $S_{\theta}$ . The initial organ surface level (h) was defined as the distance between  $P_{\theta}$  and the height of the substrate on which the organ was resting as identified from the scanning data. Thus, the relative surface displacement was calculated as the ratio of the absolute height change to the original height (i.e.,  $\frac{d}{h} \times 100\%$ ).

Real-time silent speech. Studies associated with silent speech recognition were done using 3D-printed TENG fiber-based membranes affixed to the user's face using a surgical mask. For silent speech studies, the participant said the number "three," the letter "D," or the word "print" silently (i.e., performing the physical act of speaking but without sound production) during which the short-circuit current ( $I_{SC}$ ) of the membrane was continuously monitored. The participant remained still and silent with a neutral facial expression at other times throughout the experiment. An anti-aliasing filter was designed to filter signals above the Nyquist frequency (500 Hz). Custom Matlab scripts provided communication with the data acquisition card to obtain real-time electrical signals.  $I_{SC}$  signals associated with the user's facial muscle movements were detected using a threshold method. The thresholds were determined by the frequency-domain noise level. Measurements were acquired at a sampling rate of 1000 Hz. Acquired signals were digitally filtered with a band-pass filter (0.1 to 20 Hz) and a notch filter at 60 Hz and its harmonics. Note, the notch filter was added to provide additional filtering from 60 Hz noise associated with power outlets.

To train the machine learning algorithm, we first reduced the dimensionality of the filtered signal via Principal Component Analysis (PCA) and Individual Component Analysis (ICA). Depending on the subject's jaw shape and muscle movements, we observed varying effectiveness of the dimensionality reduction. If the accuracy of prediction increased by 1% or greater, the dimensionality reduction step was utilized in the training algorithm. To obtain the classifier coefficients, we implemented various supervised learning methods and compared the accuracy rates. The methods included linear and quadratic discriminant analysis, linear, quadratic, and Gaussian support vector machine, and K-nearest Neighbor models. In the real-time feedback

system, the machine learning model that exhibited the highest degree of accuracy in the training algorithm was used.

Finite element simulations. Simulations of the triboelectric effect for the silicone-Cu system were performed using a commercially available finite element modeling software (COMSOL Multiphysics). The charge density on the silicone top surface was set at -2  $\mu$ C m<sup>-2</sup>. The electrical potential was investigated with different distances from 0 to 1 mm with a step size of 0.1 mm. The external conductive object (top) was set as the ground.

**Tensile Testing Studies.** 3D-printed TENG membranes (36 mm × 2.6 mm) were characterized in a tensile test using a mechanical testing apparatus (50 kN load cell; Model 3300; Instron). The samples were fabricated using 36 AWG Cu wires. Tensile testing was performed at a constant strain rate of 1 mm/min. The Young's modulus was obtained as the slope of the linear elastic region of the stress-strain curve. The ultimate tensile strength (UTS) was obtained as the maximum of the stress-strain curve.

### Results

**3D printing processes.** As shown in Fig. 1a, a coaxial multi-material micro-extrusion process enabled 3D printing of elastomeric metal-core triboelectric fibers. Cu wire and silicone served as the metal core and elastomeric cladding, respectively. Elastomeric metal-core silicone-Cu fibers provide attractive materials for creating self-powered wearable triboelectric devices, based on current generated by electron transfer from proximity to or mechanical contact with biological tissue, such as skin. Coaxial micro-extrusion of elastomeric silicone-Cu fibers involved a custom wire-feed manifold that enabled passive wire drawing through terminal anchoring of the fiber on the printing substrate. The micro-extrusion nozzle served as the extrusion die and

provided wire alignment and encapsulation within the elastomeric cladding. Design and fabrication details associated with the custom manifold are provided in Supplementary Fig. S1. As shown in Fig. 1b, continuous extrusion of silicone in combination with continuous vertical motion of the extruder (i.e., vertical 3D printing) resulted in the production of metal-core elastomeric silicone-Cu fibers. A photograph of the 3D-printed silicone-Cu fiber and micrograph of the fiber cross-section are shown in Figs. 1c and d, respectively. As shown in Fig. 1c, the 3D-printed silicone-Cu fibers are highly flexible, due to the low bending modulus of the Cu wire and the high elasticity of the silicone cladding. The fiber diameter (840  $\pm$  8  $\mu$ m) reasonably approximates the nozzle inner diameter (838 µm), indicating a minimal die-swell effect during extrusion. In addition to fiber 3D printing on planar stationary substrates, elastomeric metal-core fibers were also 3D printed on continuously rotating substrates. As shown in Fig. 1e, fiber printing on continuously rotating mandrels enabled the fabrication of 3D hollow structures, including cylinders and cones (see Figs. 1f and g, respectively). The process was scalable through modification of the mandrel diameter, thus enabling the fabrication of wearable systems, including wristbands (see Fig. 1h). As shown in Fig. 1i, the process also enabled the fabrication of 3D constructs on planar stationary substrates that contained distributed anchors, including cuboid- and star-shaped structures (see Figs. 1j and k, respectively). The process also offered control over the fiber and core diameters. For example, elastomeric metalcore silicone-Cu fibers were fabricated across a range of outer fiber diameters from 510 to 1,560 μm that contained Cu core diameters ranging from 79 to 320 μm, respectively. Scanning electron micrographs of fiber cross sections printed with varied core-shell sizes are shown in Supplementary Fig. S4. As shown in Fig. S4, the process resulted in an asymmetric cladding of the core wore, which is attributed to asymmetry in the wire feed mechanism. Thus, core

positioning is constrained by the die design. We remind the reader that the primary focus of this study is TENG fiber assembly into 3D and form-fitting constructs and not optimization of core position.

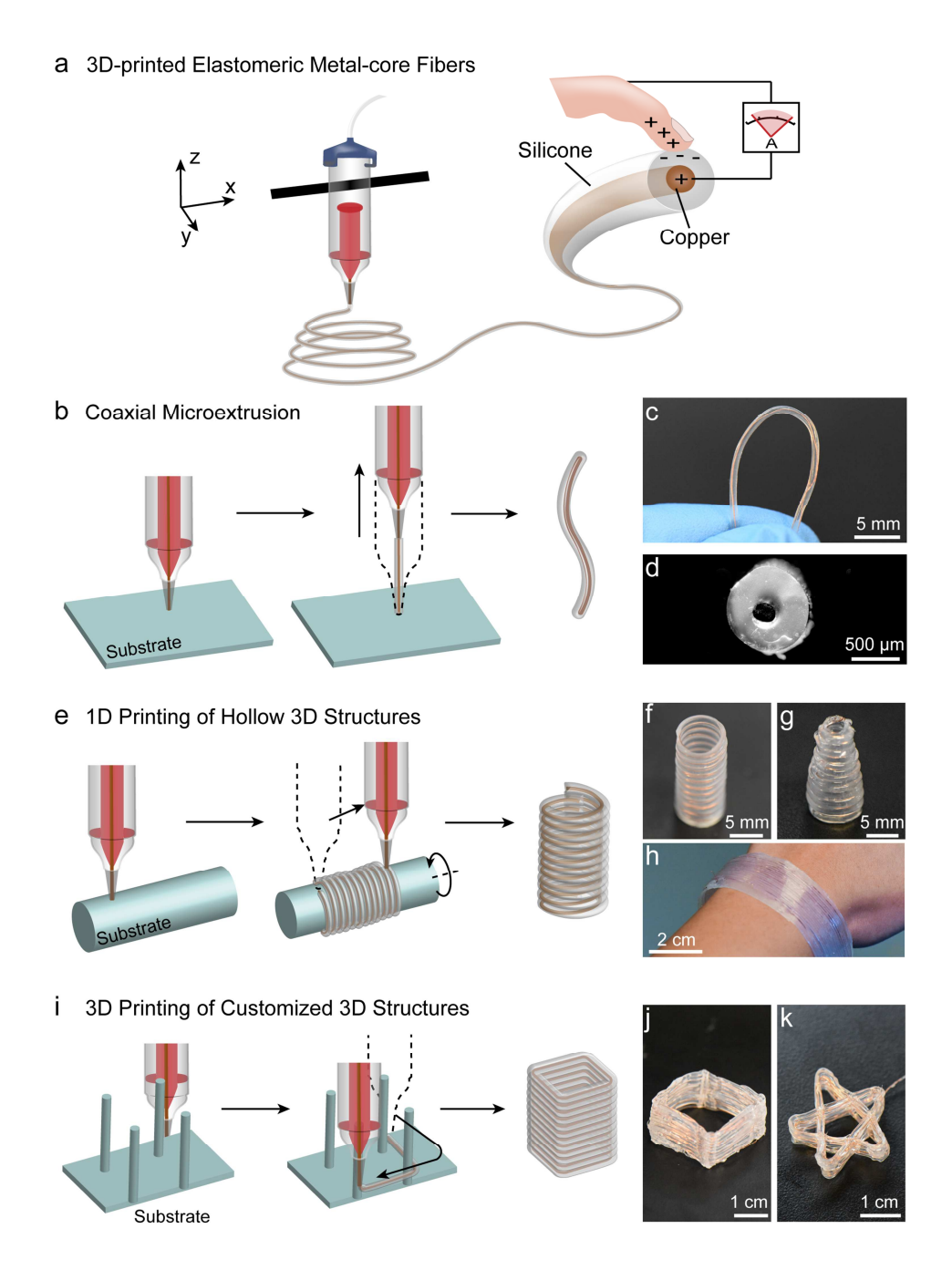


Figure 1. Description of Elastomeric Metal-core Triboelectric Fiber 3D Printing. a) Concept of 3D printing elastomeric metal-core silicone-Cu fibers. b) Schematic illustrating micro-extrusion 3D printing of silicone-Cu fibers through a terminal anchoring process. c) Photographs of flexible 3D-printed elastomeric metal-core silicone-Cu fibers. d) Micrograph of the fiber cross-section (silicone cladding, Cu core). e) Schematic illustrating the fabrication of 3D hollow

structures via 3D printing on continuously rotating substrates. Photographs of 3D-printed hollow cylinder (f) and cone (g) triboelectric constructs. h) Demonstration of device scalability through the fabrication of triboelectric wristbands. i) Schematic illustrating 3D printing on planar substrates containing distributed anchors. Photographs of 3D-printed triboelectric cuboid- (j) and star-shaped (k) structures.

Triboelectric performance. 3D-printed elastomeric metal-core silicone-Cu fibers and devices can be characterized in various measurement formats. As wearable triboelectric mechanosensors described in the following sections, the Cu wire was directly connected to the test samples (e.g., the skin or the organ), and the triboelectric fiber worked in the contact-separation mode. The working mechanism is shown in Fig. 2a. The skin served as the first triboelectric material and the ground, and the silicone cladding of the TENG fiber served as the second triboelectric material. The Cu core of the TENG fiber served as the electrode. Triboelectric fibers facilitate energy harvesting based on the coupling of triboelectrification and electrical induction effects. Silicone is among the most negatively charged materials in the triboelectric series[44], and thus, provides as an excellent candidate for wearable triboelectric devices driven via skin contact. As shown in Fig. 2a, contact between the skin and the silicone-Cu fiber results in electrons in the skin being attracted to the silicone layer of the TENG, because the latter lies in a more negative location in the triboelectric series. When the skin moves away, the accumulated negative charge on silicone induces a positive charge in the Cu wire for compensation, which creates current flow from the skin to the fiber. Similarly, when the skin re-contacts the silicone, the current returns to the skin. No current is present when equilibrium has been reached. Thus, triboelectric fibers generate alternating current associated with repetitive triboelectric charge transfer cycles, during which

the electrical potential of the Cu wire increases with decreasing separation distance between the two triboelectric materials (*e.g.*, skin and silicone). The amplitude of the induced current depends on the amount of the transferred charge and the frequency of the contact event. Static and dynamic finite element simulations of the working mechanism are shown in Fig. 2b and Video S1, respectively, in terms of the electrical potential distribution established by the two interacting triboelectric materials. As shown in Fig. 2b and Video S1, motion of the two triboelectric materials established an electrical potential distribution that drove charge transfer. When the distance between the materials decreased, the electrical potential of the Cu wire increased, and vice versa.

The triboelectric responses of single elastomeric metal-core silicone-Cu fibers (diameter = 700 µm; length = 2.5 cm) and 3D-printed wristbands (testing contact area = 1 x 1 cm<sup>2</sup>) were quantified with cyclic loading tests. A schematic of the apparatus is provided in Supplementary Fig. S2. The triboelectric responses of the single silicone-Cu fibers and 3D-printed wristbands in terms of the short-circuit current ( $I_{SC}$ ), transferred charge (Q), and open-circuit voltage ( $V_{OC}$ ) are provided in Figs. 2c-e and Figs. S5a-c, respectively. The circuit configuration used for characterization is shown in Fig. S6. The single fibers exhibited  $I_{SC}$ ,  $V_{OC}$ , and Q maxima of 0.38 µA, 5.75 V, and 2.65 nC, respectively, while the wristbands exhibited maxima of 0.46 µA, 8.01 V, and 3.97 nC, respectively. Studies were also conducted using various loads that allowed current flow to examine the corresponding power density (PD). The corresponding PD was calculated as  $PD = I^2R/A$ , where I is the current, R is the resistance of the external load, and A is the contact area. As can be seen in Figs. 2f and S5d, the single TENG fibers and 3D-printed wristbands exhibit a maximum PD of 31.39 and 23.94 mW m<sup>-2</sup>, respectively. The decreased maximum PD of the wristband relative to the single fiber is associated with the wristband's

relatively decreased Cu-to-silicone volume ratio, which caused a relatively lower induced charge for the same loading conditions.

To further verify the durability of the 3D-printed TENG fibers, a 5000-cycle loading test was performed using a force amplitude of 50 N. We selected 50 N as the applied force amplitude in the cyclic loading study based on its established use as the upper limit of the dynamic range associated with force sensors for human motion monitoring applications[45-47]. As shown in Fig. 2g, no visible decay in  $I_{SC}$  was observed after 5000 loading cycles, which indicated that the silicone-Cu TENG fibers and 3D-printed constructs could serve as reliable transducers for sensing and energy harvesting applications. We note that it is critical to examine device durability under the loading conditions expected in applications (*e.g.*, magnitude and frequency of the dynamic load)[48-49].

The circuit for a 3D-printed silicone-Cu TENG fiber-based energy harvester and the measured charging curves associated with charging of two commercial capacitors using a single silicone-Cu TENG fiber are shown in Figs. 2h and i. The voltage saturated at 55 V after 4.5 min and 10.1 min for the 0.1 and 0.22 μF capacitors, respectively. We also showed that the generated energy could be consumed instantaneously. As shown in Fig. 2j, a single silicone-Cu TENG fiber was sufficient for powering 20 LEDs. Given biomedical applications may establish humid testing environments, we also investigated the effect of humidity on the fiber output. The experimental apparatus and temporal fiber responses are shown in Fig. S7a and b, respectively. The data show that changes in relative humidity caused a minimal effect on the maximum short-circuit current, which decreased from 0.41 to 0.35 μA upon a relative humidity increase from 20% to 70%. Importantly, the fiber remained functional in the presence of humid environements.

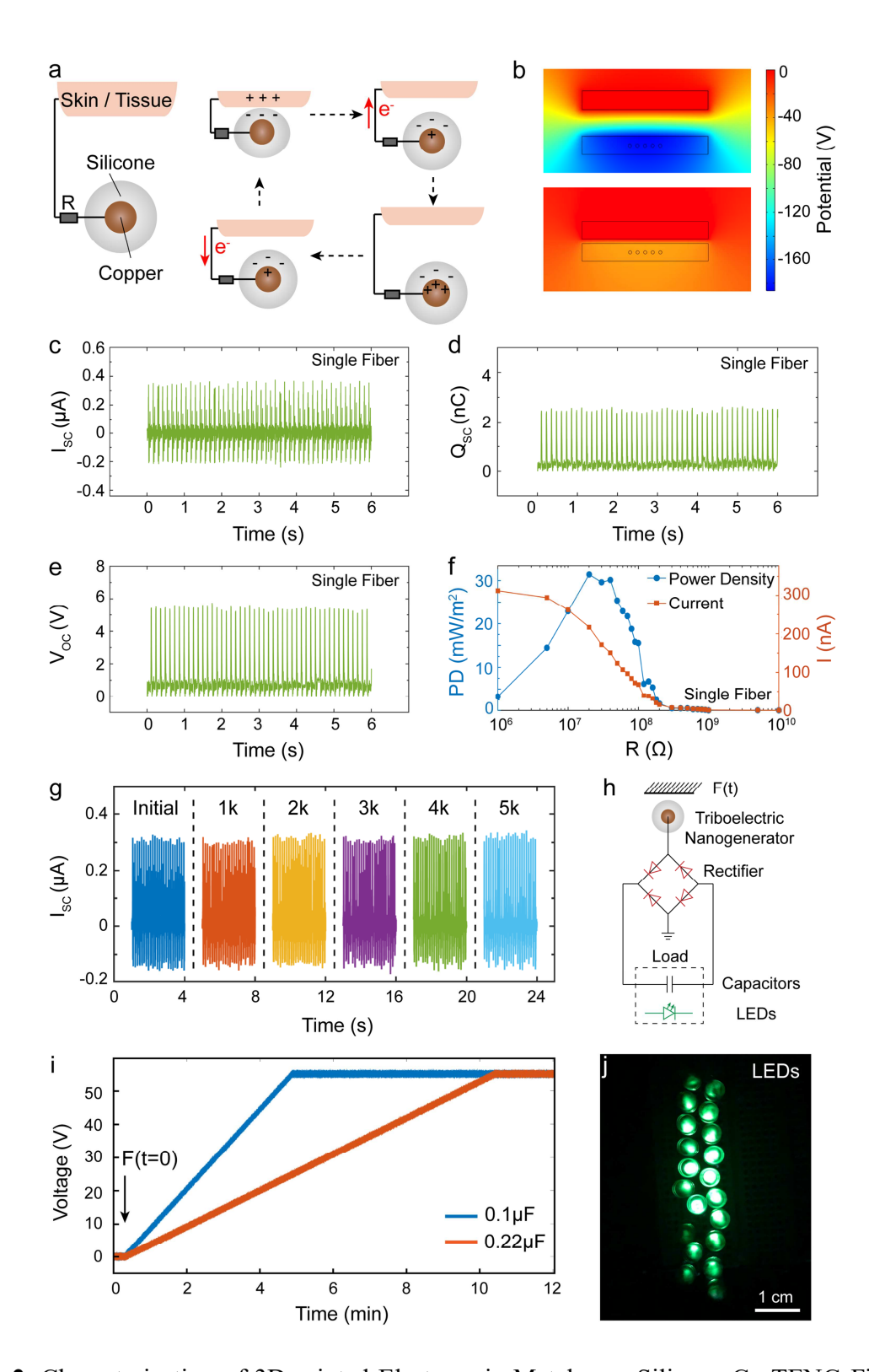


**Figure 2.** Characterization of 3D-printed Elastomeric Metal-core Silicone-Cu TENG Fiber and Device Triboelectric Performance. **a)** Schematic illustrating the working mechanism of the 3D-

printed silicone-Cu TENG fibers in the contact-separation mode. **b)** Numerical simulation of the electrical potential distribution created upon dynamic contact-separation of silicone and skin. **c-e)** Short-circuit current, transferred charge, and open-circuit voltage of the 3D-printed silicone-Cu TENG fibers under cyclic loading (contact area = 18 mm<sup>2</sup>; load = 50 N; frequency = 8 Hz). **f)** Current generated for different external loads and corresponding power densities. **g)** Short-circuit current generated in the durability tests (*i.e.*, cyclic loading studies - contact area = 18 mm<sup>2</sup>; load = 50 N; frequency = 8 Hz). **h)** Circuit for capacitor charging and LED powering using a silicone-Cu TENG fiber generator. **i)** Charging curves for two commercial capacitors using a single silicone-Cu TENG fiber. **j)** Photograph showing powering of 20 LEDs using a single silicone-Cu TENG fiber.

**Organ monitoring.** Having shown that the extruded elastomeric metal-core fibers are highly flexible, can be 3D printed in various structures, and serve as reliable TENGs, we next examined if the response of 3D-printed TENG fiber-based triboelectric devices could enable sensing of mechanical motions associated with perfusion-induced organ edema, a significant problem encountered in *ex vivo* machine perfusion-based organ preservation processes[50-51]. In addition to a suite of conformal bioanalytical devices for non-invasive isolation of biomarkers from perfused organs and biosensors for compositional analysis of perfusate and microfluidic biopsy samples[39], next-generation *ex vivo* machine perfusion systems by necessity should incorporate low-power sensors for real-time monitoring of organ edema (*i.e.*, swelling). As shown in Figs. 3a-c, the process enabled the fabrication of an organ-conforming mesh-based triboelectric mechanosensor by conformal 3D printing of TENG fibers on anatomical models of porcine kidneys. During the perfusion test, the contact area between the mesh and the kidney

dynamically change for three reasons. First, natural variance in the size and shape of kidneys from different animals establishes unavoidable discontinuities (i.e., gaps) between the mesh and the kidneys that were tested (i.e., while the mesh geometry was indeed fabricated based on a porcine kidney template, the kidney used for templating was not the same as the kidneys used for testing). Second, the fiber surfaces contain inherent variance in surface topography. Third, the organ and the silicone cladding can deform due to perfusion-induced increases in contact force. Such swelling-associated changes in the organ-mesh contact area drove electron transfer between perfused kidney and the form-fitting triboelectric sensor, thus changing the electrical potential distribution. As shown in Fig. 3d (point cloud data), the perfused kidneys swelled ~ 20% in height over the course of a 2-hour normothermic machine-perfusion interval. As shown in Fig. 3e, the real-time  $V_{OC}$  response of the sensor agreed reasonably with the surface displacement measured by 3D scanning (i.e., point cloud data) throughout the preservation interval, which contained a 5-minute baseline equilibration period (with no perfusion) followed by a 1-hour machine perfusion period. Following the 1-hour perfusion period, the perfusate flow was stopped and the kidney was continuously monitored throughout a further 1-hour post-perfusion Both the sensor  $V_{OC}$  and the kidney surface displacement increased monotonically throughout the preservation period. Stopping the perfusate flow caused a continuous decrease in both signals over the course of the next 6 min.  $V_{OC}$  increased to a maximum of  $\sim 70$  V, which occurred at the end of the perfusion period, and ultimately stabilized at  $\sim 20$  V at  $t \sim 120$  min. Kidney displacement increased by a maximum of 32.7%, which similarly occurred at the end of the perfusion period, and decreased to a value of 19.7% at the end of the post-perfusion period and in the absence of perfusate flow. While the total surface displacement and the voltage response reached a maximum value at the time at which the perfusate flow was stopped, the

voltage response of the TENG mesh stabilized ~ 10 minutes prior to the maximum of total surface displacement. This result could be attributed to various factors, including reaching the upper end of the TENG device dynamic range, change in the mechanisms by which total surface displacement affects change in device-organ contact area, or sensitivity of the TENG device to other perfusion-induced physiological changes in the perfused kidney (such as perfusion-induced injury). Given the organ swelling response was analyzed in terms of a total surface displacement, we attribute the discrepancy in rates of decrease in the sensor response and total surface displacement to changes in the top region of the kidney that did not couple with change in device-organ contact area. In summary, the data in Fig. 3e suggest that 3D-printed form-fitting constructs composed of silicone-Cu TENG fibers provide attractive self-powered, wearable mechanosensors for organ preservation and biomanufacturing applications, specifically real-time sensing of perfusion-induced edema.

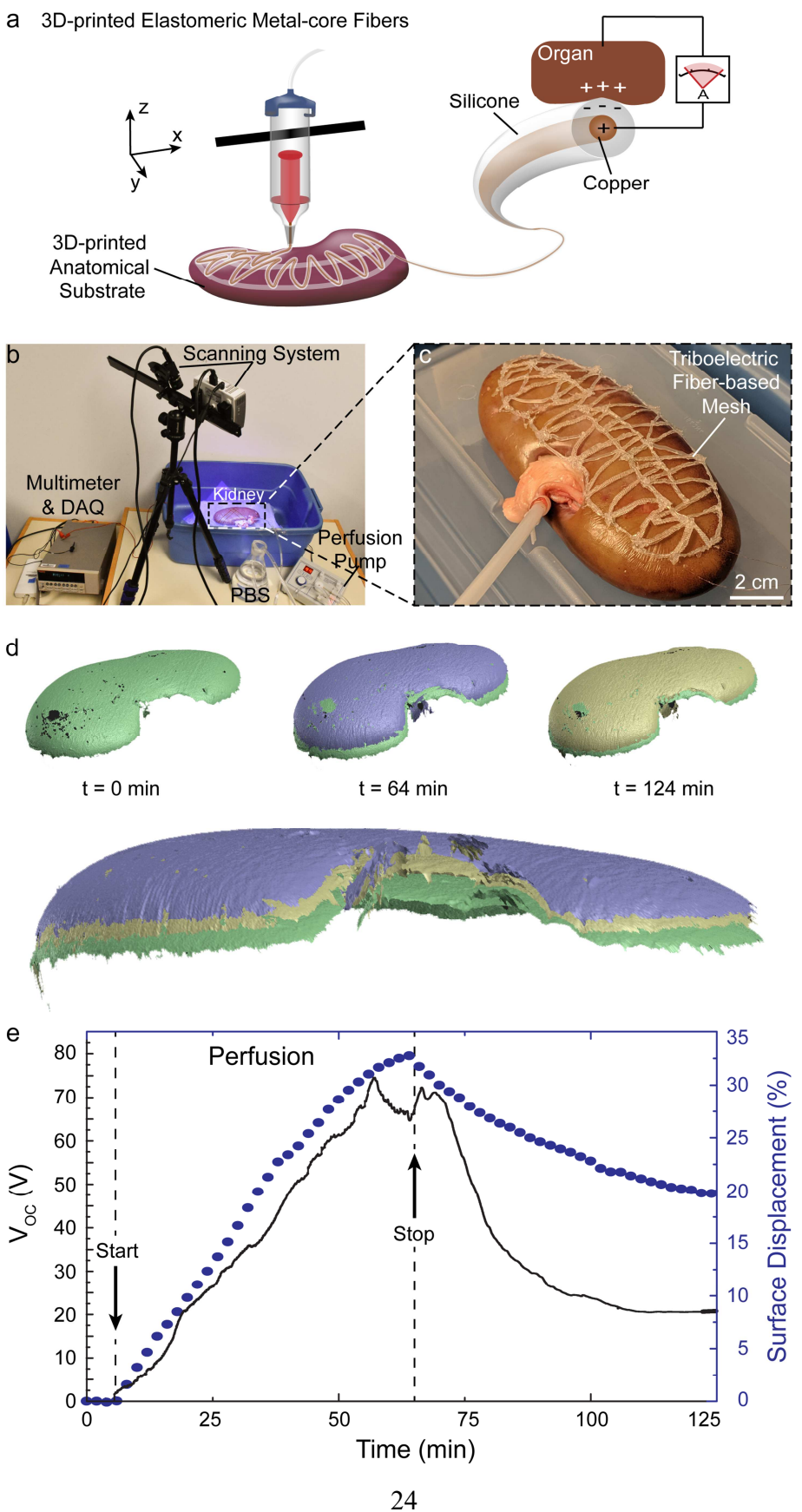


**Figure 3.** Form-fitting Organ-conforming Stretchable TENG Fiber-based Mesh for Monitoring of Perfused Organs. **a)** Schematic illustrating conformal 3D printing of elastomeric metal-core TENG fibers on objects with organic shape, specifically, a 3D-printed porcine kidney model, for fabrication of form-fitting wearable triboelectric devices. **b)** Photograph of the custom machine perfusion apparatus. **c)** Photograph of the 3D-printed kidney-conforming TENG fiber-based mesh sensor. **d)** Representative point cloud data acquired via 3D scanning of perfused porcine kidneys at t = 0 (green), 64 (purple), and 124 min (yellow). **e)** Real-time responses of organ displacement associated with perfusion-induced edema acquired using 3D scanning shown with the corresponding  $V_{OC}$  response of the 3D-printed TENG fiber-based mesh sensor.

Silent Speech. Having shown that silicone-Cu TENG fibers enabled real-time monitoring of small deformations in organs, we next examined monitoring of human activities that involve small amounts of motion. 'Silent communication,' also referred to as 'silent speech' or 'silent talk[52],' is defined as sound-free communication among humans (*i.e.*, verbal communication among humans in the absence of sound production by the speaker). We next investigated if a wearable 3D-printed triboelectric device could reliably detect and classify user speech in the absence of sound production by the speaker without the use of image-based facial expression monitoring. As shown in Figs. 4a, integration of a 3D-printed TENG fiber-based membrane (1.8 mm thick) in a surgical mask provided effective mechanical coupling between the device and the speaker's face. Movement of the user's face caused membrane deformation and thus change in device-skin contact area. Interwoven 3D-printed TENG fibers enabled the transduction of facial movements associated with silent speech to electrical response through the triboelectric effect (*e.g.*,  $I_{SC}$ ) (see Figs. 4b and c). The sensor response generated by user's facial movements were

subsequently used for real-time speech recognition via filtering, feature extraction, and classification based on the silent word spoken (the computational framework associated with speech classification is provided in Supplementary Fig. S8).

As shown in Figs. 4d and e, the 3D-printed TENG fiber-based membranes exhibited an elastic response up to engineering strains of ~20% in both vertical and horizontal directions. In contrast to single fibers, which were highly flexible but exhibited limited stretchability constrained by the elasticity of the fiber's metal core, 3D-printed constructs could be printed with toolpaths that resulted in highly stretchable devices (e.g., serpentine patterned). The mechanical properties of the TENG fiber-based membranes obtained from tensile testing studies (Young's modulus and UTS) are provided in Supplementary Table S1 and agreed with previously reported properties of 3D-printed silicone membranes[37]. While the influence of silicone-copper adhesion was not observed in the tensile testing studies, additional material processing techniques could be used for improving silicone-copper adhesion strength for applications that may generate asymmetric strain in the core and cladding materials. For example, plasma treatment of copper and other metals can be used to improve the adhesion strength of polymer coatings, including epoxy resins and organopolysiloxanes[53-54].

Fig. 4f shows the raw sensor data generated through the cumulative triboelectric effect in the sensor, which contained 60, 120, and 180 Hz noise. The filtered data corresponding to the user speaking the number "three," the letter "D," and the word "print" with no sound production are presented in Figs. 4g-i. Each sound produced a distinguishable waveform, suggesting that the platform may provide opportunities for silent speech-based communication by combination with time-series data classification methods. The observation of distinguishable signals

associated with each of the three sounds (three, D, print) was consistent among multiple human subjects (n = 3).

We trained various supervised machine learning models to classify each word that was silently spoken, including Linear Discriminant Analysis, Linear Support Vector Machine (SVM), Quadratic SVM, Gaussian SVM, and K-nearest Neighbors models. Various models, including Linear SVM, Quadratic SVM, Gaussian SVM, and K-nearest Neighbors, enabled recognition of the silently spoken word (*i.e.*, word classification in the absence of sound production by the speaker) with greater than 95% accuracy. The Linear Discriminant Analysis model exhibited the lowest word classification accuracy of 74.8%. The Quadratic SVM, Linear SVM, and K-nearest Neighbor models exhibited relatively higher word classification accuracies of 98.4, 98.4, and 98.1%, respectively. The Gaussian SVM model yielded the highest word classification accuracy of 99.2%. Fig. 4j illustrates the effect of the training sample size on the word classification accuracy for the Gaussian SVM model. Word classification accuracies exceed 95% accuracy for training sample sizes greater than 85 samples. A video demonstrating use of the 3D-printed triboelectric sensor for real-time 'silent speech' is provided in Supplementary Information (Video S2).

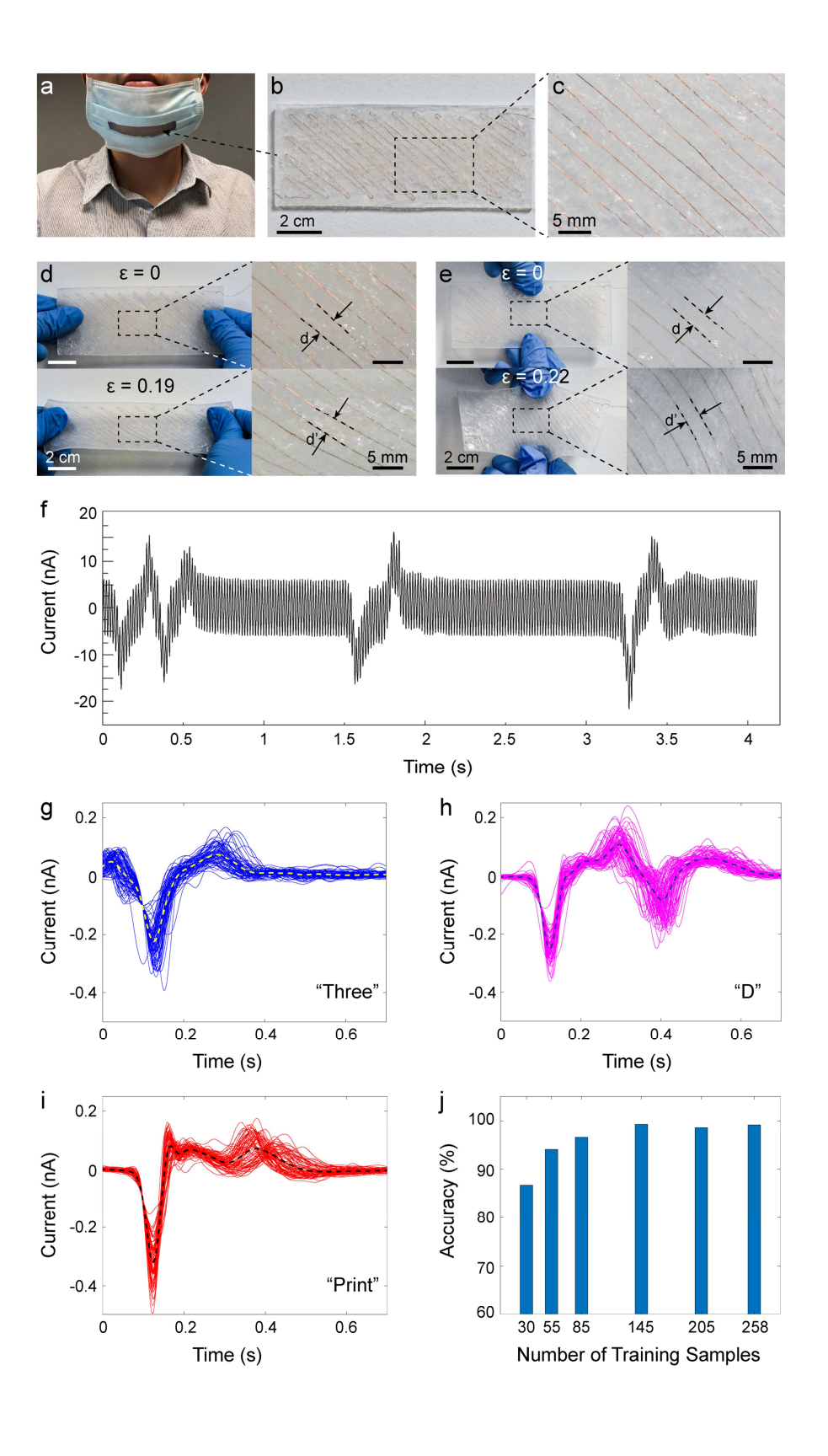


**Figure 4.** 3D-printed Stretchable Wearable TENG fiber-based Membrane for 'Silent Speech' (*i.e.*, speech recognition in the absence of sound production by the speaker). **a)** Photograph of a human subject wearing the triboelectric membrane-integrated facemask. **b)** Photograph of the stretchable TENG fiber-based membrane's integrated transduction elements (TENG fibers) with a zoomed view (**c**). **d-e)** Highlights of the TENG fiber-based membrane orthogonal stretchability with zoomed views showing fiber orientation in the absence and presence of strain. **f)** Raw sensor data generated by the worn triboelectric device during silent speech. **g-i)** Filtered and averaged (dotted line) triboelectric responses corresponding to silently speaking the number "three," the letter "D," and the word "print." **j)** Accuracy of the online classification system for different training sample sizes.

### **Discussion**

The coaxial micro-extrusion wire encapsulation process provides a unique capability for producing fibers with elastomeric claddings. Silicone and Cu were selected as the cladding and core, respectively, based on their relative positions in the triboelectric series. For example, silicone rubber is among the most negatively changed materials in the triboelectric series, while skin is among the most positively charged materials[44, 55]. The 3D-printed conformal mesh also exhibits advantages relative to the use of shape-adaptive membrane TENGs for organ monitoring applications. First, while shape-adaptive membranes can conform to objects with simple organic shape, such as the arm, they must be crumpled or folded to conform with objects that exhibit complex organic shape, such as internal organs[56-59]. In contrast, the 3D-printed conformal mesh can fit accurately with objects that exhibit complex organic shape as they are fabricated based on a template of the object. Second, conductive liquids or coated metal

nanowires are usually employed as electrodes to maintain both elasticity and conductivity in shape-adaptive membranes[56-57, 59-60], which increases the device cost and internal resistance. Alternatively, the elasticity resides in the space between adjacent fibers for the case of the 3D-printed TENG mesh, which enables the metal core to serve as the electrode and results in a relatively decreased device cost and internal resistance. Thus, elastomeric metal-core silicone-Cu TENG fibers provide attractive material properties for wearable triboelectric systems.

In addition to the large negative charge of silicone, making it an excellent candidate for triboelectric devices, silicone is an elastomer, which offers desirable mechanical properties in resultant fibers and devices. For example, as shown in Figs. 1c and 4d, silicone claddings lead to highly flexible single TENG fibers and stretchable 3D-printed triboelectric devices. As shown in Figs. 4d and e, the 3D-printed triboelectric membranes with serpentine toolpaths exhibited an elastic response up to an engineering strain ( $\Delta L/L_0$ ) of ~20%, where  $\Delta L$  is the length change and  $L_0$  is the initial length. Silicone claddings also offer improved biomechanical matching characteristics relative to other fibers. For example, the Young's modulus of silicone is 440 kPa[37], which is in the range of the Young's modulus of skin (E = 420 - 850 kPa)[61] and lower than other thermoplastic claddings, such as polysulfone ( $E \sim 2,600$  kPa).

The rheological properties of elastomers makes them excellent candidates for micro-extrusion 3D printing. For example, elastomers can exhibit Herschel-Bulkley rheological properties, defined as a power-law fluid with a yield stress. Uncured silicone elastomers can exhibit yield stresses that are sufficient to enable 3D printing of free-standing constructs. In addition to desirable rheological properties, silicone also exhibits high self adhesion and substrate adhesion, which facilitates layer-by-layer assembly of 3D structures and conformal 3D printing, respectively. As shown in Figs. 1 and 3, silicone-Cu TENG fibers can be assembled

into various structures and form factors via 3D printing, including 3D constructs and form-fitting systems. When considering the material and mechanical properties of the silicone-Cu TENG fiber system, this work represents an advance in 3D printing of fiber-based functional materials and devices, which commonly exhibit single-fiber or woven device formats composed of fibers with relatively more rigid thermoplastic claddings.

The continued, unmet demand for high-quality transplantable organs, such as kidneys, remains a driving force for the creation of novel organ preservation processes and sensors for real-time monitoring of organs[62], from real-time organ bioanalysis to real-time characterization of organ biophysical and mechanical properties. Perfusion-induced organ edema (swelling) remains an important problem for organ preservation. While edema during the reperfusion phase is expected, excessive edema is detrimental to organ health[63]. Kidneys, as highly vascularized organs, will swell during perfusion caused by the reintroduction of fluid and tissue edema[63]. In Fig. 3, we showed that 3D-printed TENG fiber-based meshes enabled real-time monitoring of machine perfused kidney swelling response (up to increases of 32.7%). The observed swelling response associated with perfusion-induced edema is consistent with previous reports[63]. The advantages of this 3D-printed triboelectric sensor in an organ preservation setting are self-powering capability, form-fitting design, and a real-time monitoring capability (sampling rate = 1 kHz). The detection of organ swelling during machine perfusion could allow interventions that may lead to better organ preservation.

Systems for silent communication, such as silent speech interfaces, have various applications, including assisted communication among the soldiers and individuals affected by speech-related disabilities[52, 64-65]. A silent speech interface is traditionally defined as a device that allows speech communication without using the sound made when individuals

vocalize their speech sounds, regardless of whether sound is produced. The most commonly used silent speech interfaces are based on simultaneous monitoring of sound production and facial expression. Thus, they require high-dimensional image data and image processing methods, which are typically computationally intensive, as well as the use of imaging systems for facial monitoring, which increases power demands, creates the need for conventional power supplies, and limits system portability and human integration. Alternatively, 3D-printed silicone-Cu TENG fiber-based devices provide a self-powered wearable system for silent speech that offers various advantages, such as those associated with wearability, durability, power consumption, and compatibility with data-driven signal processing methods, such as machine learning. Overall, 3D-printed silicone-Cu TENG fiber-based devices provide attractive systems for silent speech without the need for sound production or image-based facial expression monitoring.

### **Conclusion**

In conclusion, we report a process for 3D printing elastomeric metal-core TENG fibers based on the silicone-Cu system. The process enabled rapid prototyping of self-powered wearable triboelectric systems. The utility and sensitivity of 3D-printed silicone-Cu TENG fibers and resultant triboelectric devices was demonstrated through applications to mechanosensing in organ and human activity monitoring. 3D-printed wearable triboelectric devices and supervised learning algorithms enabled high-accuracy real-time 'silent speech' (*i.e.*, speech in the absence of sound production by the user and image-based facial expression monitoring). Ultimately, the ability to 3D print elastomeric metal-core TENG fibers on stationary or moving planar and non-planar substrates has broad implications in the fabrication of wearable triboelectric devices.

## Acknowledgments

XJ acknowledges the support of the National Science Foundation under Grant No. 1847436. BNJ acknowledges the support of the National Science Foundation (CBET-1650601).

## **Competing Interest Statement**

The authors have no competing interests to report.

# **Author Contributions**

YT, ZF, XJ, and BNJ conceived the concept of 3D printable elastomeric metal-core multifunctional fibers. YT and BNJ created the triboelecric fiber 3D printing process. YT and ZF designed and fabricated the fibers and devices. ZF, JK, and YT performed the characterization studies, data analysis, and supervised learning. JR, YT, and BNJ designed the organ monitoring studies and analyzed the organ edema data. YT, ZF, XJ, and BNJ conceived concepts of monitoring organ deformations and 'silent speech' via triboelectric sensing. YT, ZF, XJ, and BNJ organized, wrote, and edited the manuscript.

## References

- [1] Y. C. Lai, J. Deng, S. L. Zhang, S. Niu, H. Guo, and Z. L. Wang, Single thread based wearable and highly stretchable triboelectric nanogenerators and their applications in cloth based self powered human interactive and biomedical sensing, Adv. Funct. Mater. 27 (2017) 1604462.
- [2] S. Choi, H. Lee, R. Ghaffari, T. Hyeon, and D. H. Kim, Recent advances in flexible and stretchable bio electronic devices integrated with nanomaterials, Adv. Mater. 28 (2016) 4203-4218.
- [3] Y. Khan, A. E. Ostfeld, C. M. Lochner, A. Pierre, and A. C. Arias, Monitoring of vital signs with flexible and wearable medical devices, Adv. Mater. 28 (2016) 4373-4395.
- [4] X. Cao, Y. Jie, N. Wang, and Z. L. Wang, Triboelectric nanogenerators driven self□powered electrochemical processes for energy and environmental science, Adv. Energy Mater. 6 (2016) 1600665.
- [5] F. R. Fan, W. Tang, and Z. L. Wang, Flexible nanogenerators for energy harvesting and self powered electronics, Adv. Mater. 28 (2016) 4283-4305.
- [6] W. Zeng, L. Shu, Q. Li, S. Chen, F. Wang, and X. M. Tao, Fiber □ based wearable electronics: a review of materials, fabrication, devices, and applications, Adv. Mater. 26 (2014) 5310-5336.
- [7] Q. Zhang, Z. Zhang, Q. Liang, F. Gao, F. Yi, M. Ma, Q. Liao, Z. Kang, and Y. Zhang, Green hybrid power system based on triboelectric nanogenerator for wearable/portable electronics, Nano Energy 55 (2019) 151-163.
- [8] X. Pu, L. Li, M. Liu, C. Jiang, C. Du, Z. Zhao, W. Hu, and Z. L. Wang, Wearable self□charging power textile based on flexible yarn supercapacitors and fabric nanogenerators, Adv. Mater. 28 (2016) 98-105.
- [9] H. J. Sim, C. Choi, S. H. Kim, K. M. Kim, C. J. Lee, Y. T. Kim, X. Lepró, R. H. Baughman, and S. J. Kim, Stretchable Triboelectric Fiber for Self-powered Kinematic Sensing Textile, Sci. Rep. 6 (2016) 35153.

- [10] K. Dong, Y.-C. Wang, J. Deng, Y. Dai, S. L. Zhang, H. Zou, B. Gu, B. Sun, and Z. L. Wang, A highly stretchable and washable all-yarn-based self-charging knitting power textile composed of fiber triboelectric nanogenerators and supercapacitors, ACS Nano 11 (2017) 9490-9499.
- [11] W. Gong, C. Hou, Y. Guo, J. Zhou, J. Mu, Y. Li, Q. Zhang, and H. Wang, A wearable, fibroid, self-powered active kinematic sensor based on stretchable sheath-core structural triboelectric fibers, Nano Energy 39 (2017) 673-683.
- [12] X. He, Y. Zi, H. Guo, H. Zheng, Y. Xi, C. Wu, J. Wang, W. Zhang, C. Lu, and Z. L. Wang, A Highly Stretchable Fiber-Based Triboelectric Nanogenerator for Self-Powered Wearable Electronics, Adv. Funct. Mater. 27 (2017) 1604378.
- [13] A. Yu, X. Pu, R. Wen, M. Liu, T. Zhou, K. Zhang, Y. Zhang, J. Zhai, W. Hu, and Z. L. Wang, Core–shell-yarn-based triboelectric nanogenerator textiles as power cloths, ACS Nano 11 (2017) 12764-12771.
- [14] K. Dong, J. Deng, W. Ding, A. C. Wang, P. Wang, C. Cheng, Y. C. Wang, L. Jin, B. Gu, and B. Sun, Versatile core—sheath yarn for sustainable biomechanical energy harvesting and real □ time human □ interactive sensing, Adv. Energy Mater. 8 (2018) 1801114.
- [15] J. Park, D. Kim, A. Y. Choi, and Y. T. Kim, Flexible single-strand fiber-based woven-structured triboelectric nanogenerator for self-powered electronics, APL Mater. 6 (2018) 101106.
- [16] M. Zhu, M. Lou, I. Abdalla, J. Yu, Z. Li, and B. Ding, Highly shape adaptive fiber based electronic skin for sensitive joint motion monitoring and tactile sensing, Nano Energy (2020) 104429.
- [17] Y.-C. Lai, J. Deng, S. L. Zhang, S. Niu, H. Guo, and Z. L. Wang, Single-Thread-Based Wearable and Highly Stretchable Triboelectric Nanogenerators and Their Applications in Cloth-Based Self-Powered Human-Interactive and Biomedical Sensing, Adv. Funct. Mater. 27 (2017) 1604462.
- [18] K. Dong, X. Peng, and Z. L. Wang, Fiber/Fabric Based Piezoelectric and Triboelectric Nanogenerators for Flexible/Stretchable and Wearable Electronics and Artificial Intelligence, Adv. Mater. (2019) 1902549.

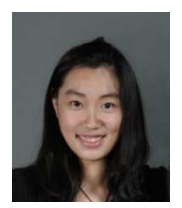
- [19] J. Xiong and P. S. Lee, Progress on wearable triboelectric nanogenerators in shapes of fiber, yarn, and textile, Sci. Technol. Adv. Mate. 20 (2019) 837-857.
- [20] A. Joe Lopes, E. MacDonald, and R. B. Wicker, Integrating stereolithography and direct print technologies for 3D structural electronics fabrication, Rapid Prototyp. J. 18 (2012) 129-143.
- [21] E. Macdonald, R. Salas, D. Espalin, M. Perez, E. Aguilera, D. Muse, and R. B. Wicker, 3D printing for the rapid prototyping of structural electronics, IEEE Access 2 (2014) 234-242.
- [22] D. Espalin, D. W. Muse, E. MacDonald, and R. B. Wicker, 3D Printing multifunctionality: structures with electronics, Int. J. Adv. Manuf. Tech. 72 (2014) 963-978.
- [23] B. Chen, W. Tang, T. Jiang, L. Zhu, X. Chen, C. He, L. Xu, H. Guo, P. Lin, and D. Li, Three-dimensional ultraflexible triboelectric nanogenerator made by 3D printing, Nano Energy 45 (2018) 380-389.
- [24] S. Gao, Y. Zhu, Y. Chen, M. Tian, Y. Yang, T. Jiang, and Z. L. Wang, Self-power electroreduction of N2 into NH3 by 3D printed triboelectric nanogenerators, Mater. Today 28 (2019) 17-24.
- [25] M. S. Mannoor, Z. Jiang, T. James, Y. L. Kong, K. A. Malatesta, W. O. Soboyejo, N. Verma, D. H. Gracias, and M. C. McAlpine, 3D printed bionic ears, Nano Lett. 13 (2013) 2634-2639.
- [26] Y. L. Kong, M. K. Gupta, B. N. Johnson, and M. C. McAlpine, 3D printed bionic nanodevices, Nano Today 11 (2016) 330-350.
- [27] J. Z. Gul, B.-S. Yang, Y. J. Yang, D. E. Chang, and K. H. Choi, In situ UV curable 3D printing of multi-material tri-legged soft bot with spider mimicked multi-step forward dynamic gait, Smart Mater. Struct. 25 (2016) 115009.
- [28] D. Lei, B. Luo, Y. Guo, D. Wang, H. Yang, S. Wang, H. Xuan, A. Shen, Y. Zhang, and Z. Liu, 4-Axis printing microfibrous tubular scaffold and tracheal cartilage application, Sci. China Mater. 62 (2019) 1910-1920.
- [29] S. Z. Guo, K. Qiu, F. Meng, S. H. Park, and M. C. McAlpine, 3D printed stretchable tactile sensors, Adv. Mater. 29 (2017) 1701218.

- [30] P. Laszczak, L. Jiang, D. L. Bader, D. Moser, and S. Zahedi, Development and validation of a 3D-printed interfacial stress sensor for prosthetic applications, Med. Eng. Phys. 37 (2015) 132-137.
- [31] Y. Tong, E. Kucukdeger, J. Halper, E. Cesewski, E. Karakozoff, A. P. Haring, D. McIlvain, M. Singh, N. Khandelwal, and A. Meholic, Low-cost sensor-integrated 3D-printed personalized prosthetic hands for children with amniotic band syndrome: A case study in sensing pressure distribution on an anatomical human-machine interface (AHMI) using 3D-printed conformal electrode arrays, PLoS One 14 (2019) e0214120.
- [32] S. Chen, T. Huang, H. Zuo, S. Qian, Y. Guo, L. Sun, D. Lei, Q. Wu, B. Zhu, and C. He, A Single Integrated 3D□Printing Process Customizes Elastic and Sustainable Triboelectric Nanogenerators for Wearable Electronics, Adv. Funct. Mater. 28 (2018) 1805108.
- [33] Y. L. Kong, I. A. Tamargo, H. Kim, B. N. Johnson, M. K. Gupta, T.-W. Koh, H.-A. Chin, D. A. Steingart, B. P. Rand, and M. C. McAlpine, 3D printed quantum dot light-emitting diodes, Nano Lett. 14 (2014) 7017-7023.
- [34] M. Saari, B. Cox, E. Richer, P. S. Krueger, and A. L. Cohen, Fiber encapsulation additive manufacturing: An enabling technology for 3D printing of electromechanical devices and robotic components, 3D Print. Addit. Manuf. 2 (2015) 32-39.
- [35] Y. Tong, J. M. Murbach, V. Subramanian, S. Chhatre, F. Delgado, D. C. Martin, K. J. Otto, M. Romero-Ortega, and B. N. Johnson, A hybrid 3D printing and robotic-assisted embedding approach for design and fabrication of nerve cuffs with integrated locking mechanisms, MRS Adv. 3 (2018) 2365-2372.
- [36] J. M. Murbach, S. Currlin, A. Widener, Y. Tong, S. Chhatre, V. Subramanian, D. C. Martin, B. N. Johnson, and K. J. Otto, In situ electrochemical polymerization of poly (3, 4-ethylenedioxythiophene)(PEDOT) for peripheral nerve interfaces, MRS Commun. 8 (2018) 1043-1049.
- [37] B. N. Johnson, K. Z. Lancaster, G. Zhen, J. He, M. K. Gupta, Y. L. Kong, E. A. Engel, K. D. Krick, A. Ju, and F. Meng, 3D printed anatomical nerve regeneration pathways, Adv. Funct. Mater. 25 (2015) 6205-6217.

- [38] B. N. Johnson, K. Z. Lancaster, I. B. Hogue, F. Meng, Y. L. Kong, L. W. Enquist, and M. C. McAlpine, 3D printed nervous system on a chip, Lab Chip 16 (2016) 1393-1400.
- [39] M. Singh, Y. Tong, K. Webster, E. Cesewski, A. P. Haring, S. Laheri, B. Carswell, T. J. O'Brien, C. H. Aardema, and R. S. Senger, 3D printed conformal microfluidics for isolation and profiling of biomarkers from whole organs, Lab Chip 17 (2017) 2561-2571.
- [40] K. Wang, G. Ouyang, X. Chen, and H. Jakobsen, Engineering electroactive dielectric elastomers for miniature electromechanical transducers, Polym. Rev. 57 (2017) 369-396.
- [41] K. Parida, V. Kumar, W. Jiangxin, V. Bhavanasi, R. Bendi, and P. S. Lee, Highly transparent, stretchable, and self□healing ionic□skin triboelectric nanogenerators for energy harvesting and touch applications, Adv. Mater. 29 (2017) 1702181.
- [42] Y. C. Lai, J. Deng, S. Niu, W. Peng, C. Wu, R. Liu, Z. Wen, and Z. L. Wang, Electric eel □skin □ inspired mechanically durable and super □stretchable nanogenerator for deformable power source and fully autonomous conformable electronic □skin applications, Adv. Mater. 28 (2016) 10024-10032.
- [43] S. Li, W. Peng, J. Wang, L. Lin, Y. Zi, G. Zhang, and Z. L. Wang, All-elastomer-based triboelectric nanogenerator as a keyboard cover to harvest typing energy, ACS Nano 10 (2016) 7973-7981.
- [44] H. Zou, Y. Zhang, L. Guo, P. Wang, X. He, G. Dai, H. Zheng, C. Chen, A. C. Wang, and C. Xu, Quantifying the triboelectric series, Nat. Commun. 10 (2019) 1-9.
- [45] S. Wang, L. Gong, Z. Shang, L. Ding, G. Yin, W. Jiang, X. Gong, and S. Xuan, Novel Safeguarding Tactile e□Skins for Monitoring Human Motion Based on SST/PDMS–AgNW–PET Hybrid Structures, Adv. Funct. Mater. 28 (2018) 1707538.
- [46] Z. Zhang, K. Du, X. Chen, C. Xue, and K. Wang, An air-cushion triboelectric nanogenerator integrated with stretchable electrode for human-motion energy harvesting and monitoring, Nano Energy 53 (2018) 108-115.
- [47] T. Li, H. Luo, L. Qin, X. Wang, Z. Xiong, H. Ding, Y. Gu, Z. Liu, and T. Zhang, Flexible capacitive tactile sensor based on micropatterned dielectric layer, Small 12 (2016) 5042-5048.

- [48] X. Wang, J. Sun, L. Dong, C. Lv, K. Zhang, Y. Shang, T. Yang, J. Wang, and C.-X. Shan, Stretchable and transparent electroluminescent device driven by triboelectric nanogenerator, Nano Energy 58 (2019) 410-418.
- [49] N. Zhang, C. Qin, T. Feng, J. Li, Z. Yang, X. Sun, E. Liang, Y. Mao, and X. Wang, Non-contact cylindrical rotating triboelectric nanogenerator for harvesting kinetic energy from hydraulics, Nano Res. (2020) 1-5.
- [50] M. J. Taylor and S. C. Baicu, Current state of hypothermic machine perfusion preservation of organs: The clinical perspective, Cryobiology 60 (2010) S20-S35.
- [51] E. E. Guibert, A. Y. Petrenko, C. L. Balaban, A. Y. Somov, J. V. Rodriguez, and B. J. Fuller, Organ preservation: current concepts and new strategies for the next decade, Transfus. Med. Hemother. 38 (2011) 125-142.
- [52] B. Denby, T. Schultz, K. Honda, T. Hueber, J. M. Gilbert, and J. S. Brumberg, Silent speech interfaces, Speech Commun. 52 (2010) 270-287.
- [53] J. N. Borges, T. Belmonte, J. Guillot, D. Duday, M. Moreno Couranjou, P. Choquet, and H. N. Migeon, Functionalization of copper surfaces by plasma treatments to improve adhesion of epoxy resins, Plasma Process Polym. 6 (2009) S490-S495.
- [54] G. Costantino, D. B. Zeik, and S. J. Clarson, Improvement of the adhesion of silicone to aluminum using plasma polymerization, J. Inorg. Organomet. Polym. 4 (1994) 425-430.
- [55] J. Chen and Z. L. Wang, Reviving vibration energy harvesting and self-powered sensing by a triboelectric nanogenerator, Joule 1 (2017) 480-521.
- [56] X. Pu, M. Liu, X. Chen, J. Sun, C. Du, Y. Zhang, J. Zhai, W. Hu, and Z. L. Wang, Ultrastretchable, transparent triboelectric nanogenerator as electronic skin for biomechanical energy harvesting and tactile sensing, Sci. Adv. 3 (2017) e1700015.
- [57] R. Liu, X. Kuang, J. Deng, Y. C. Wang, A. C. Wang, W. Ding, Y. C. Lai, J. Chen, P. Wang, and Z. Lin, Shape memory polymers for body motion energy harvesting and self□powered mechanosensing, Adv. Mater. 30 (2018) 1705195.

- [58] Q. Zheng, Y. Zou, Y. Zhang, Z. Liu, B. Shi, X. Wang, Y. Jin, H. Ouyang, Z. Li, and Z. L. Wang, Biodegradable triboelectric nanogenerator as a life-time designed implantable power source, Sci. Adv. 2 (2016) e1501478.
- [59] J. Deng, X. Kuang, R. Liu, W. Ding, A. C. Wang, Y. C. Lai, K. Dong, Z. Wen, Y. Wang, and L. Wang, Vitrimer elastomer □ based jigsaw puzzle □ like healable triboelectric nanogenerator for self □ powered wearable electronics, Adv. Mater. 30 (2018) 1705918.
- [60] F. Yi, X. Wang, S. Niu, S. Li, Y. Yin, K. Dai, G. Zhang, L. Lin, Z. Wen, and H. Guo, A highly shape-adaptive, stretchable design based on conductive liquid for energy harvesting and self-powered biomechanical monitoring, Sci. Adv. 2 (2016) e1501624.
- [61] M. Pawlaczyk, M. Lelonkiewicz, and M. Wieczorowski, Age-dependent biomechanical properties of the skin, Adv. Dermatol. Allergol. 30 (2013) 302.
- [62] D. Eshmuminov, D. Becker, L. B. Borrego, M. Hefti, M. J. Schuler, C. Hagedorn, X. Muller, M. Mueller, C. Onder, and R. Graf, An integrated perfusion machine preserves injured human livers for 1 week, Nat. Biotechnol. (2020) 1-10.
- [63] K. E. Webster, "Quantifying Renal Swelling during Machine Perfusion using Digital Image Correlation," Virginia Tech, 2017.
- [64] T. Hueber, E.-L. Benaroya, G. Chollet, B. Denby, G. Dreyfus, and M. Stone, Development of a silent speech interface driven by ultrasound and optical images of the tongue and lips, Speech Commun. 52 (2010) 288-300.
- [65] K. Brigham and B. V. Kumar, "Imagined speech classification with EEG signals for silent communication: a preliminary investigation into synthetic telepathy," 4<sup>th</sup> iCBBE, 2010, pp. 1-4.



Yuxin Tong received her B.E. degree in Aerospace Engineerig (2015) from Beihang
University and M.S. in Industrial and Systems Engineering from Virginia Tech (2015). She is
currently a Ph.D. candidate in the Grado Department of Industrial and Systems Engineering.
Her research is focused on the design and manufacturing of wearable sensors and form-fitting devices.



**Ziang Feng** received his B.S. degree in Optical Information Science and Technology and MEng degree in Optical Engineering from Beijing Jiaotong University in China in 2012 and 2015, respectively. He is currently a Ph.D. candidate in the Bradley Department of Electrical and Computer Engineering at Virginia Tech. His research interests include energy harvesting, multimaterial fibers, and fiber-optic sensors.



Jongwoon Kim receieved his B.A. degree in Physics at Ohio Wesleyan University (2015), B.S. and M.S. degree in Electrical Systems Engineering at Washington University in St. Louis (2018). He is currently a Ph. D. candidate in the Bradley Department of Electrical and Computer Engineering at Virginia Tech. His research interests include multimaterial fibers and signal processings for biomedical applications.



John Robertson is a Professor in the Biomedical Engineering Department at Virginia Tech. His research is focused on organ transplantation, organ preservation, tissue engineering, and translational cancer research. He received his B.S. degree in Biology (1969) and M.S. degree in Zoology (1973) from the State University of New York - Stony Brook and M.S. degree in Pathology (1973), V.M.D. degree in Vetrinary Medicine (1976), and Ph.D. degree in Medical Pathology from the University of Pennsylvania (1977). He has received various honors and awards in the fields of pathology and toxicology.



Xiaoting Jia is an assistant professor in the Department of Electrical and Computer Engineering at Virginia Tech. Her research focuses on multimaterial fibers for wearable and biomedical applications. Before joining Virginia Tech, she was a postdoc associate in the Research Laboratory of Electronics at MIT. She received her Ph.D. in Materials Science and Engineering from MIT (2011), M.S. in Materials Science and Engineering from Stony Brook University (2006), and B.S. in Materials Science from Fudan University in China (2004). She is a recipient of NSF CAREER award, 3M Non-Tenured Faculty Award, and the Translational Fellow at MIT.



Blake Johnson is an assistant professor in the Department of Industrial and Systems

Engineering at Virginia Tech. His research focuses on biosensing and biomanufacturing.

Before joining Virginia Tech (2015), he was a postdoctoral associate in the Department of

Mechanical and Aerospace Engineering at Princeton University. He received his B.S. degree
in Chemical Engineering from the University of Wisconsin-Madision (2008) and Ph.D.

degree in Chemical Engineering from Drexel University (2013). He is the recipient of the

Outstanding Young Investigator Award from the Institute of Industrial and Systems

Engineering (IISE) Manufacturing and Design Division and SME Outstanding Young

Manufacturing Engineer Award.

Declaration of interests
oximes The authors declare that they have no known competing financial interests or personal relationships that could have appeared to influence the work reported in this paper.
⊠The authors declare the following financial interests/personal relationships which may be considered as potential competing interests:
N/A